ACS OMEGA

Open Access

http://pubs.acs.org/journal/acsodf

Article

Nonclassical Pathways: Accelerated Crystal Growth of Sodium Hexafluorosilicate Microrods via Nanoparticle-Assisted Processes with 0D Silicon Quantum Dots

Maheswari Palanivel, Devaraj Nataraj,* Thankappan Thrupthika, Subramaniam Ramya, Sellan Premkumar, and T. Daniel Thangadurai

Cite This: *ACS Omega* 2024, 9, 24060−24070

Read Online

ACCESS | Metrics & More | Article Recommendations | Supporting Information

ABSTRACT: Nonclassical crystallization represents an innovative pathway that utilizes nanoparticles, enabling the generation of single crystals, going beyond a classical mechanism dependent on atoms, ions, or molecules. Our investigation has revealed hierarchical structures emerging via the aggregation and fusion of primary silicon quantum dots (SiQDs). In contrast to the classical ion-by-ion crystallization process, the primary SiQDs initially undergo aggregation, followed by fusion and their subsequent crystallization, leading to the ultrafast crystal growth of sodium hexafluorosilicate (SHFS) microrods with diverse morphologies. A comprehensive fluorescence microscopy study is performed to examine the mechanism of microrod formation through the primary aggregation and fusion of SiQDs at room temperature in the presence of hydrogen fluoride (HF). The different concentrations of HF play a crucial role in the formation of flower-, block-, and hexagonal-shaped SHFS microrods. However, the presence of a high-concentration HF causes a reduction in microrod size, elucidated through a range of analytical and spectroscopic techniques.

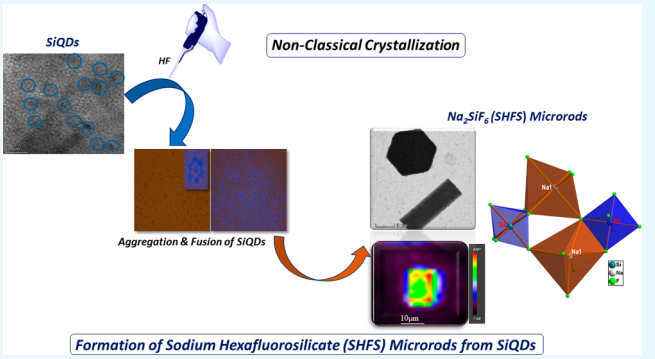

1. INTRODUCTION

Crystal growth is a fundamental phenomenon which is observed in various areas of research including physics, chemistry, and biology. It has wide interest in both the natural and synthetic worlds.[1−3] For example, crystallization is a spontaneous process found in many living organisms from the formation of shells to the construction of skeletal support.[4−6] Also, various man-made industrial materials can be designed by the crystallization process.[7,8] The crystallization can be divided into two categories such as (i) classical crystallization and (ii) nonclassical crystallization (NCC). In the classical model, the crystals are grown by the layer-by-layer arrangement of atoms and ions. A unit cell consists of a group of atoms, and the repetition of the unit cell can result in the formation of the required crystal system. The large particles grow by the addition of ions supplied at the expense of small particles in the chemical synthesis route. This is a well-known Ostwald ripening process.[9−11] In contrast, the atoms and ions are not involved in the nonclassical crystallization process. It is nothing but the process of "crystallization through particle attachment".[12−14]

Oriented attachment (OA) is a nonclassical crystallization process driven by interparticle assembly and oriented fusion, often leading to the formation of single-crystalline nanostructures with controlled morphologies and properties. This aggregation-based growth mechanism occurs at the mesoscopic scale (10−100 nm), where individual nanoparticles merge along specific crystallographic directions.[12,15] OA offers a versatile approach for tailoring the electronic, optical, and catalytic properties of various materials, including lead sulfide (PbS). For example, the oriented attachment of PbS nanoparticles in two dimensions has been shown to yield ultrathin single-crystal sheets with enhanced photoconductive behavior.[17] Similarly, catalyst-free PbSe nanorods with tailored optoelectronic properties were fabricated through OA.[18] The real-time-oriented attachment was observed in ZnO nanoparticle.[19]

In conclusion, OA presents a powerful tool for the bottom-up construction of advanced nanomaterials with precisely controlled functionalities. The oriented attachment (OA) mechanism, implemented in sol−gel and wet-chemical synthesis routes, provides a versatile approach for creating metal

Received: March 27, 2024
Revised: April 19, 2024
Accepted: April 24, 2024
Published: May 21, 2024

Scheme 1. Schematic Representation of the Formation of Na_2SiF_6 Microrods (SHFS) from SiQDs

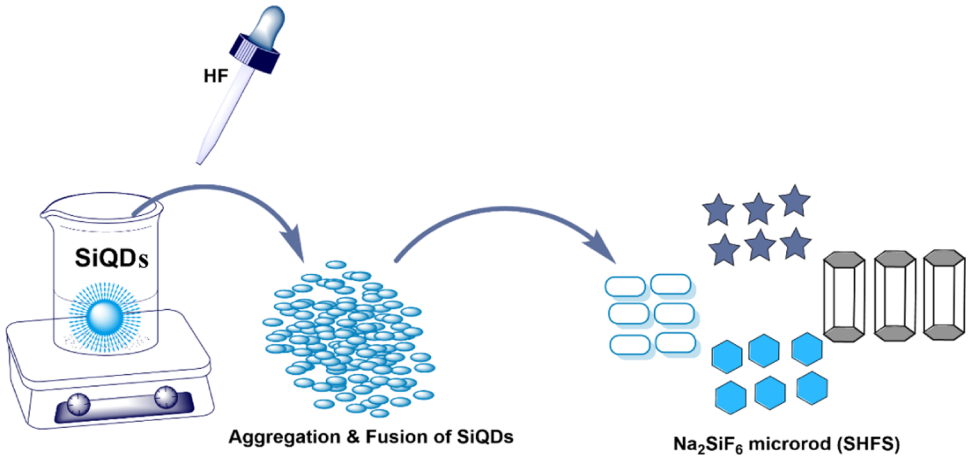

oxide nanowires with a controlled size and diverse morphologies. This is exemplified by the synthesis of MnO multipods through OA within the sol–gel process.[20] Similarly, CuO nanowires were successfully fabricated by manipulating the self-assembly and crystallization of $Cu(OH)_2$ nanocrystals using the same method.[21] The hydrothermal approach also leverages OA for nanomaterial synthesis, typically employing surfactants, moderate-to-low temperatures, and extended reaction times. This method was demonstrated to facilitate the ultrafast aggregation of SnO_2 nanocrystals into bulk crystals within 180 h.[22] Notably, the resulting self-assembled nanomaterials, formed through aggregation, hold considerable potential for constructing functional nanoscale devices.

Nonclassical crystallization techniques have been successfully employed to synthesize a diverse array of novel materials featuring intricate morphologies or hierarchical structures. These materials have found applications in various fields including catalysis, gas sensing, energy storage, environmental remediation, and beyond. The synthesis of sodium hexafluorosilicate (SHFS) through nonclassical crystallization processes can significantly reduce synthesis timeframes. Sodium hexafluorosilicate exhibits unique properties that make it valuable in the ceramic, chemical, and electronic industries. It possesses commendable chemical, physical, and optical characteristics. Notably, Mn-doped sodium hexafluorosilicate shows promise for applications in warm white light-emitting diode (LED) technology,[20] further underlining the versatility and potential of nonclassical crystallization methods for designing materials for advanced technological applications.[14,20]

This work presents novel findings on the nonclassical crystallization of silicon quantum dots (SiQDs) facilitated by sodium hexafluorosilicate (SHFS) microrods within a hydrofluoric acid (HF) solution. The process unfolds through discernible stages, each modulated by varying HF concentrations, diverging from conventional nucleation and growth mechanisms. The size, shape, and crystal structure of SHFS microrods were affected by HF addition. The morphology of SiQD aggregates transitions from flower-like structures to hexagonal SHFS microrods with increasing HF concentrations, suggesting controlled morphological evolution linked to HF levels (Scheme 1). Achieving a maximum HF concentration of 1.5 mL ensured the optimal crystallinity of hexagonal SHFS microrods, as confirmed by powder X-ray diffraction (PXRD). The crystal structure of SHFS microrods is characterized using single-crystal X-ray diffraction (XRD), while energy-dispersive X-ray spectroscopy (EDS) analysis maps Si, O, Na, and F element intensities. Elucidation of the SHFS microrod formation mechanism from SiQDs is conducted by using fluorescence microscopy. Additionally, the exciton relaxation pathways of both SiQDs and SHFS microrods are investigated through steady-state and time-resolved spectroscopy techniques.

These findings highlight the crucial role of HF concentration in shaping the crystallization process of SiQDs, shedding light on the captivating nonclassical aspects of this phenomenon. The implications of these results are thoroughly discussed in this study, contributing valuable insights into the scientific community.

2. EXPERIMENTAL SECTION

2.1. Materials. (3-Aminopropyl) triethoxysilane (≥98%, Sigma-Aldrich), trisodium citrate dehydrate (99–100% anhydrous, purchased from Sigma-Aldrich), and hydrogen fluoride (48%, Loba Chemie) were the materials used in this study. Double distilled water (DDI) was utilized for the preparation of aqueous solutions.

2.2. Synthesis of SiQDs and SHFS Microrods. *2.2.1. Synthesis of SiQDs.* The synthesis of SiQDs was carried out based on a previously reported method with slight modifications.[23] Briefly, 0.25 g of trisodium citrate was dispersed in 30 mL of distilled water. Subsequently, 0.8 mL of the silicon source (3-aminopropyl triethoxysilane) was slowly added, and the mixture was stirred for 15 min. The resulting precursor solution was transferred into a 40 mL Teflon-lined stainless-steel autoclave and heated at 180 °C for 12 h. After the reaction, the autoclave was cooled to room temperature. The formation of SiQDs was indicated by the resulting light-yellow-colored solution.

2.2.2. Synthesis of SHFS Microrods. SHFS microrods were synthesized by mixing 10 mL of SiQDs with different concentrations (0.1–0.5, 1, and 1.5 mL) of hydrogen fluoride (HF) and stirring continuously for 5 min until the light-yellow solution turned transparent, indicating the formation of SHFS microrods.

2.3. Structural and Morphological Analysis. X-ray diffraction measurements were conducted by using a Rigaku Smartlab analytical instrument. The SiQDs and SHFS microrods solution were drop-cast onto a glass substrate with an area of 1 cm^2. After drying, the films were analyzed by XRD. Single-crystal X-ray diffraction data were collected on a Rigaku

https://doi.org/10.1021/acsomega.4c02952
ACS Omega 2024, 9, 24060–24070

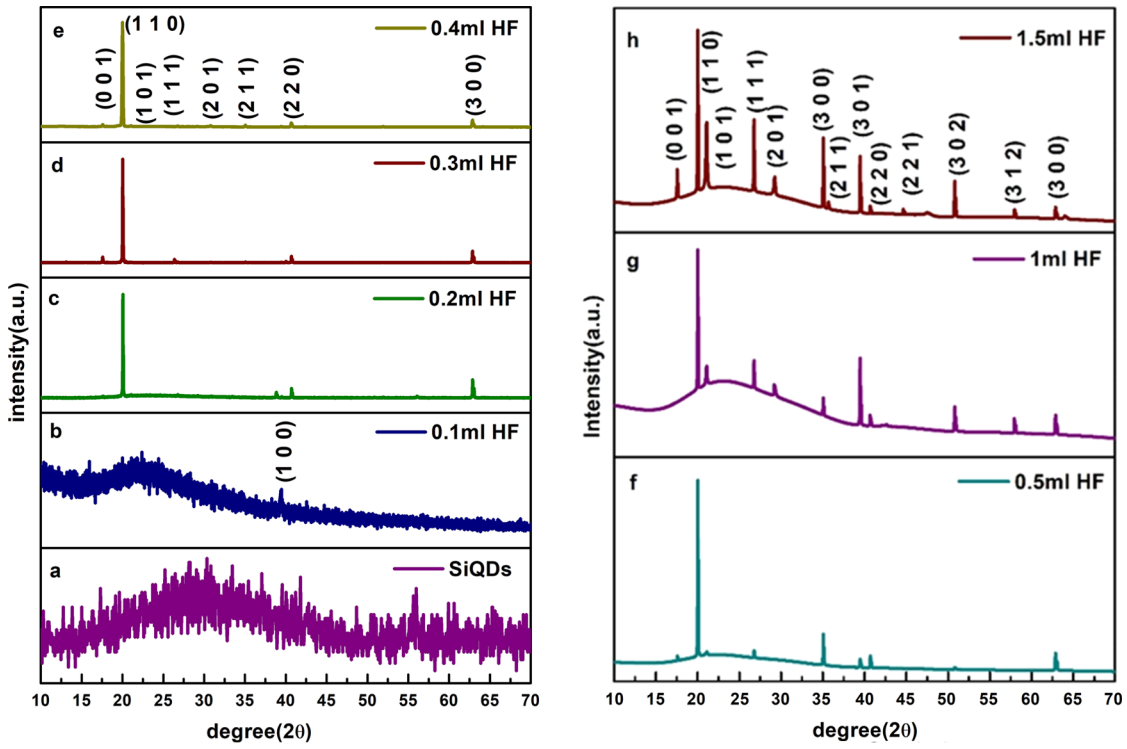

Figure 1. PXRD patterns of film-dried SiQDs and SHFS microrods formation at different concentrations of HF. (a) PXRD pattern of the SiQDs. (b) Aggregation of silica nanoparticle along with the NaF particles. (c) Sodium hexafluorosilicate and NaF particle. (d−h) Present only sodium hexafluorosilicate.

Saturn 724+ CCD diffractometer equipped with a microfocus Mo Kα (λ = 0.7107 Å) radiation source for unit cell determination and three-dimensional (3D) intensity data collection. High-resolution transmission electron microscopy (HR-TEM) analysis was performed using a THEMIS 300 G3 instrument operating at 300 kV. Samples were drop-cast onto carbon-coated copper grids (200 mesh) and used for the measurements. Field-emission scanning electron microscopy (FESEM) analysis was conducted with a JEOL JSM-7600F instrument. Samples were drop-cast onto a glass slide, coated with platinum as a conductive material using a sputter coater, and then analyzed by FESEM. Raman spectra were recorded using a Horiba LABRAM HR instrument excited by a 532 nm laser. The samples were drop-cast onto a glass substrate, and after drying, the films were analyzed by Raman spectroscopy. Raman in-depth profile and mapping were recorded using a Renishaw instrument excited by a 532 nm laser.

2.3.1. Optical Measurements. An Agilent Cary 60 spectrophotometer with a 10 mm quartz cuvette was used to measure the absorption of both the SiQDs and the SHFS microrod structure in deionized water. All absorption experiments were carried out at room temperature. The baseline correction for all absorption spectra was performed by using deionized water (DI water) before the measurements. Steady-state photoluminescence (PL) emission was measured by using a Horiba Jobin Yvon Fluoromax-4 spectrofluorometer, maintaining an excitation/emission slit width of 2 nm. Time-dependent photoluminescence analysis of SiQDs and the SHFS microrod structure was performed by using a time-correlated single-photon counting (TCSPC) system with a 365 nm excitation wavelength. The decay traces were analyzed using the data analysis software IBH DAS v6.2.

3. RESULTS AND DISCUSSION

In this study, we present a straightforward method for synthesizing one-dimensional sodium hexafluorosilicate (SHFS) microrods from zero-dimensional silicon quantum dots (SiQDs) through a nanoparticle-mediated, nonclassical ultrafast crystallization process induced by hydrofluoric acid (HF) treatment. The SHFS microrod formation process involves two steps. Initially, SiQDs are synthesized by using a hydrothermal method. Subsequently, the prepared SiQDs sample undergoes treatment with an HF solution. Following the HF treatment, the SiQDs aggregate and fuse, resulting in the formation of SHFS microrods, as depicted in Figure 1. Notably, the crystallinity of the SHFS increases with the rising HF concentration in the SiQDs solution. Figure 1a displays the X-ray diffraction (XRD) patterns of the obtained SiQDs. Two broad diffraction peaks observed at 28.40 and 56.30° correspond to the (111) and (311) crystallographic planes of cubic-phase SiQDs (JCPDS no: 895012), respectively.[24] The calculated average crystalline size using the Scherer equation is 4.34 ± 0.1 nm. Initially, the SiQDs solution has a pH of 10, indicating an alkaline nature. However, upon introducing a small amount of HF (0.1 mL) into the SiQDs solution, amorphous silica nanoparticles and NaF are generated, leading to a decrease in the solution's pH to 6. The diffraction peak at 39° corresponds to the (100) crystallographic plane of NaF (JCPDS no: 89-2659).[25−27] Further addition of HF (0.2 mL) to the SiQD solution results in new peaks at pH 5, corresponding to the (110), (221), and (300) crystallographic planes of SHFS (JCPDS 33-1280), along with the NaF diffraction peaks. As the HF concentration is progressively decreased from the pH level 5 to 1 in increments of 0.3, 0.4, 0.5, 1.0, and 1.5 mL, the following peaks are observed: (001), (110), (101), (111), (201), (300), (211), (301), (220), (221),

https://doi.org/10.1021/acsomega.4c02952
ACS Omega 2024, 9, 24060−24070

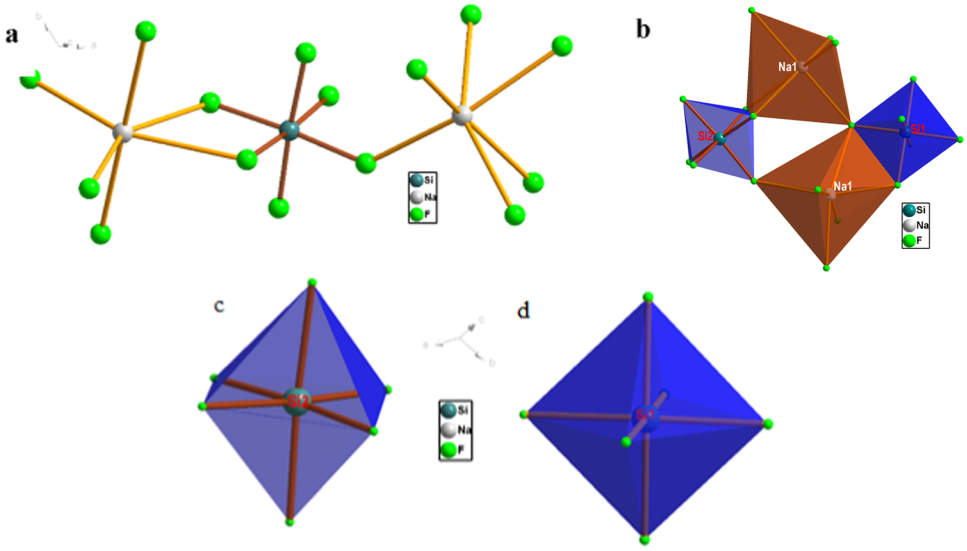

Figure 2. (a) Molecular structures of Na_2SiF_6. (b) Polyhedron model of $[NaF_6]^{5-}$ (brown) and $[SiF_6]^{2-}$ (blue). (c) The distorted octahedral (bottom-left) and (d) octahedral (bottom-right) configuration of $[SiF_6]^{2-}$ groups.

(302), (312), and (300) crystallographic planes (JCPDS no: 33-1280), indicating the hexagonal structure of SHFS.[28,29] These results suggest a significant increase in the purity of the SHFS microrods in solution with increasing HF concentration. In the sample treated with 1.5 mL HF, the intensity of the diffraction peak at 21.12°, corresponding to the (101) plane of Na_2SiF_6, is the highest, indicating the preferred growth direction.

3.1. Molecular Structures of SHFS Microrod. Single crystals of Na_2SiF_6 with X-ray quality were obtained by slow evaporation of a solution containing SiQDs in HF at room temperature. The microrod crystallizes in the trigonal, noncentrosymmetric (NCS) space group *P*321.[30] The molecular structure of Na_2SiF_6 is depicted in Figure 2a,b. The crystal structure of Na_2SiF_6 consists of two crystallographically independent sodium cations and two distinct $[SiF_6]^{2-}$ octahedra. Six NaF_6 octahedra are interconnected, dividing the edges to form hexapetaloid shapes, and the centers of these petals create hexagonal channels in which Si atoms are located (Figure 2). The $[Si(2)F_6]^{2-}$ octahedron is composed of six identical Si−F bonds (1.670 (9) Å) (Figure 2d), while the $[Si(1)F_6]^{2-}$ octahedron has two different Si−F bonds with bond lengths of 1.684 (12) and 1.682 (10) Å. The F−Si−F angles are approximately 91 and 179°, respectively, indicating that the $[Si(2)F_6]^{2-}$ octahedron exhibits a slightly distorted geometry (Figure 2c).

To investigate the structural and morphological changes of SiQDs and SHFS, we conducted HR-TEM analysis on the images shown in Figure 3a,b. The HR-TEM images clearly depict the agglomeration of SiQDs, indicating that the sample comprises ultrasmall spherical SiQDs with an average size of 4.06 ± 0.1 nm (Figure S2). Notably, Figure 3b illustrates unique lattice fringes with an interplanar spacing of 0.31 nm, corresponding to the (111) plane of diamond silicon.[31,32] The selected area electron diffraction shows good crystallinity of the SiQDs (Figure S1). Additionally, the STEM-EDS elemental mapping of Si, Na, and O in the SiQDs agglomeration is shown in Figure 4b−d.

Similarly, the SHFS microrods, observed in TEM images (Figure 5a,b), are significantly larger than the QDs, with a size of approximately 700 nm. Certain areas of the sample exhibit

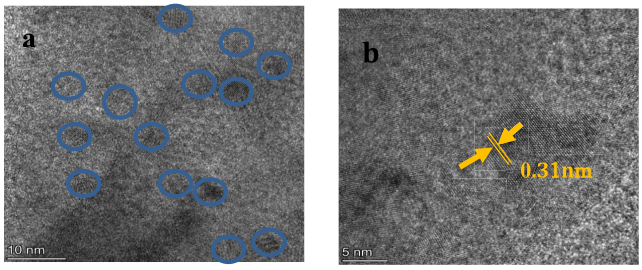

Figure 3. (a) Representative bright field HR-TEM image of 5 nm SiQDs. (b) High-resolution TEM of SiQDs showing lattice fringes of 0.31 nm characteristics of the (111) plane.

clusters of SHFS, as shown in HR-TEM image (Figure 5c). The elemental mapping of Si, Na, and F in the SHFS microrod is shown in Figure 6a−e.

In the field-emission scanning electron microscopy (FESEM) analysis, SHFS microrods exposed to incremental HF concentrations (shown in Figure 7a−i) demonstrate varied morphologies. In fluorescence microscopy analysis, initially at 0.1 mL HF, small silica particles are evident. The introduction of 0.2 mL HF leads to a self-assembly of these particles into flower-like structures. The increment of the HF to 0.3 mL results in a transition to hexagonal morphologies (Figure S7A−D). The addition of 0.4 mL HF induces aggregation and fusion among flower-shaped particles, evolving into block-shaped structures (Figure S3) and the elemental mapping shows the presence of Si, Na, and F in the block-shaped SHFS microrods (Figure S4). The rod sizes are observed to increase with further HF concentration increments. Specifically, at 0.5 mL of HF, uniform-sized rods are visible (Figure 7a−c), and at 1 mL of HF, there is a noticeable decrease in rod size (Figure 7d−f). Elevating the HF to 1.5 mL yields hexagonal rods of moderate length and greater width compared to lower HF concentrations (Figure 7g,h), albeit with reduced size uniformity beyond 1 mL of HF. This pattern aligns with nanoparticle-mediated nonclassical crystal growth theory for SHFS microrod development from SiQDs. Elemental mapping through FESEM (Figure 8b−d) has verified the presence of elemental composition in the microrods. The small SHFS

https://doi.org/10.1021/acsomega.4c02952
ACS Omega 2024, 9, 24060−24070

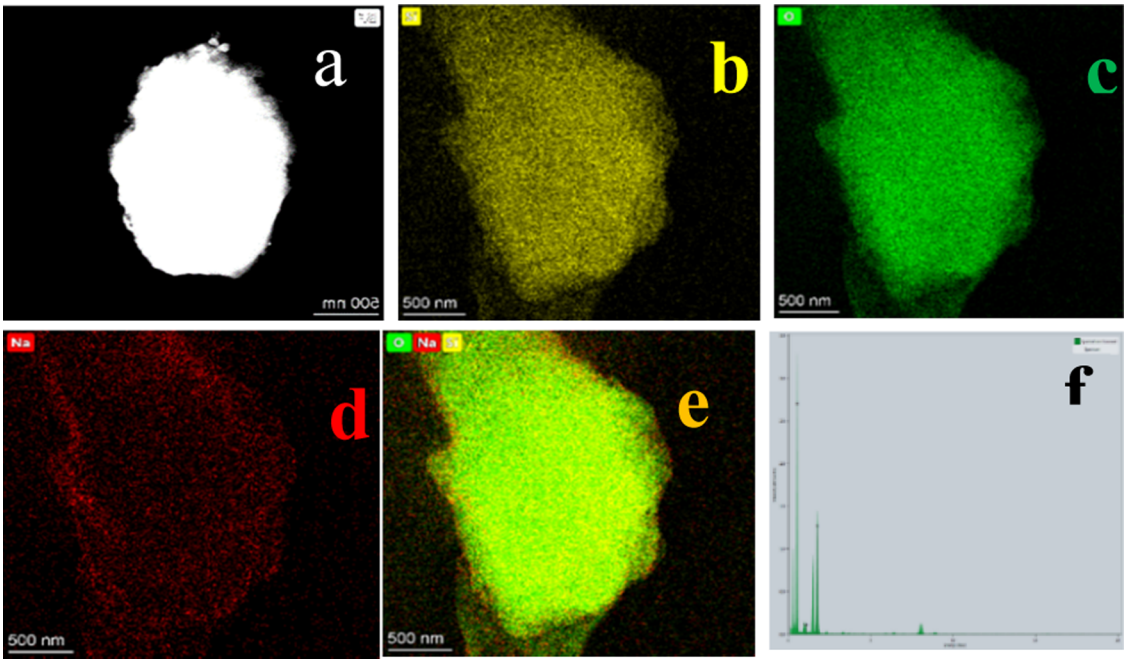

Figure 4. (a) Elemental mapping from STEM images of SiQDs and its corresponding elemental mapping images of (b) Si, (c) O, (d) Na, (e) Si, O, Na, and (f) STEM-EDS atomic ratio of Si, O, Na.

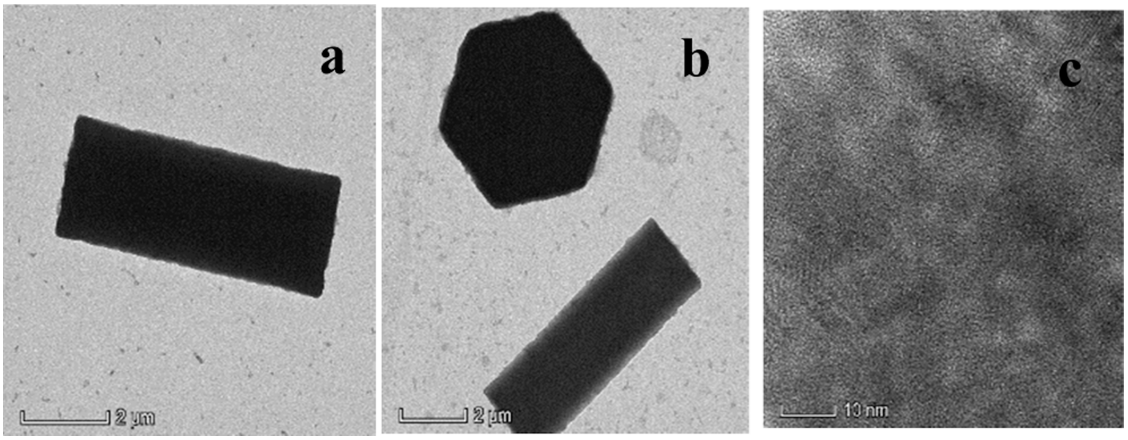

Figure 5. (a–b) TEM shows the sodium hexafluorosilicate microrod (SHFS) and (c) HR-TEM shows the SHFS cluster.

microrods exhibit diminished fluorescence and aggregation at higher concentrations of HF (2–5 mL) (Figure S8).

Raman spectroscopy was utilized to explore the surface structural evolution from silicon quantum dots (SiQDs) to sodium hexafluorosilicate (SHFS) microrods. Comparative analysis of SiQDs and SHFS microrods revealed distinct surface characteristics. Figure 9 illustrates the Raman spectra of SiQDs, while Figure 10(a–g) presents the spectra obtained from various HF concentrations, detailing the formation of SHFS microrods. These spectra were acquired using a confocal microprobe Raman spectroscopy technique with a 532 nm excitation wavelength. The Raman microscopy images of SHFS rod formation is shown in Figures S5 and S6.

In SiQDs, observed bands at 450, 550, and 790 cm^{-1} are attributed to the motion of oxygen in Si–O–Si stretching and bending modes. Additionally, a broad band at 1090 cm^{-1} is assigned to Si–O stretching modes in various SiO_4 tetrahedral forms, commonly classified as Qn species, where "*n*" indicates the number of nonbridging oxygen atoms per SiO_4 tetrahedron. Specifically, the Q3 species at 1000 cm^{-1} corresponds to SiO_4 tetrahedra with three nonbridging oxygen atoms.[33−36]

The introduction of a minimal HF volume (0.1 mL) to SiQDs resulted in two distinctive peaks at 560 and 780 cm^{-1}, representing Si–O–Si stretching and bending vibrations. A slight increase in wavenumber highlighted SiQDs aggregation, as shown in Figure 10a. An additional 0.2 mL of HF introduced a new band at 654 cm^{-1}, corresponding to Si–F vibration, indicative of SHFS's flower-like morphology aggregation, as depicted in Figure 10b. This suggests that the observed morphological changes are primarily due to the Si–F bond formation. With further HF concentration increase (0.3–1.5 mL), the nanoparticles gradually transitioned into sodium hexafluorosilicate microrods, exhibiting Raman vibrational bands at 410, 480, and 663 cm^{-1}, labeled as $\nu 1$, $\nu 2$, and $\nu 5$, respectively. These modes are associated with various vibrational modes of $(SiF_6)^{2-}$. $\nu 1$ denotes the symmetric stretching vibration of Si–F within $(SiF_6)^{2-}$. $\nu 2$ corresponds to the

https://doi.org/10.1021/acsomega.4c02952
ACS Omega 2024, 9, 24060−24070

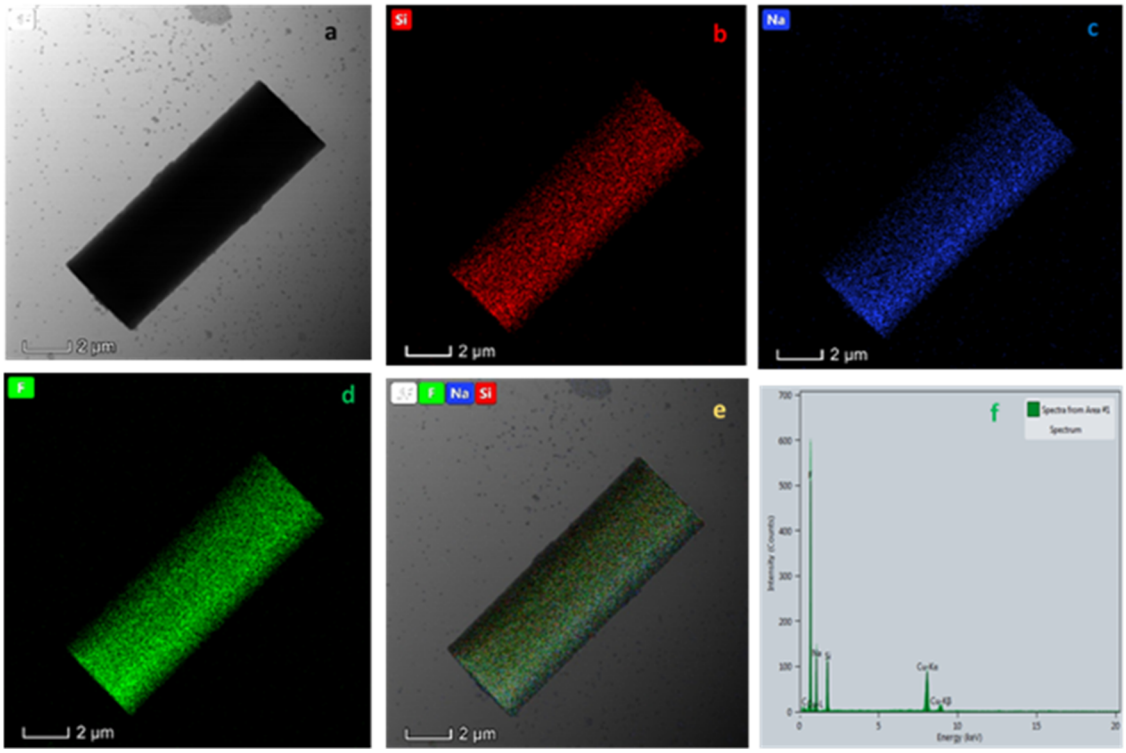

Figure 6. (a) Bright field TEM images of SHFS microrod and its corresponding elemental mapping images (b) Si, (c) Na, (d) F, (e) Si, Na, F, and (f) STEM-EDS atomic ratio of Si, Na, F.

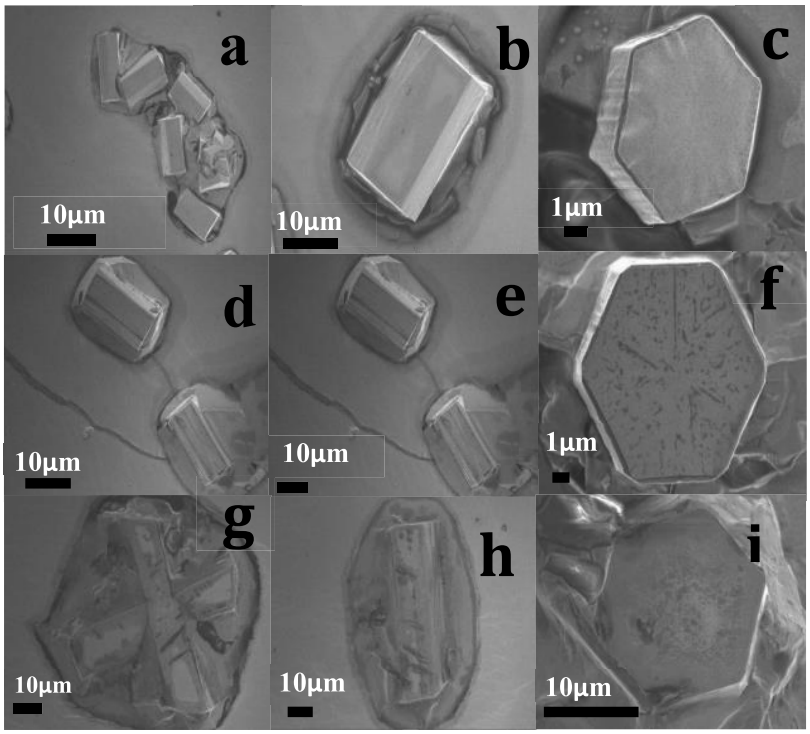

Figure 7. (a–c) FESEM images illustrating the growth of the SHFS microrods in 0.5 mL of HF concentration. (d–f) 1 mL of HF concentration for SHFS microrod size is decreased. (g–i) The SHFS microrod and hexagonal shape decrease when the HF concentration is 1.5 mL.

bending vibration of Si–F, and $\nu 5$ represents Si–F stretching vibrational modes in SHFS microrods (Figure 10d–g). The vibrational modes $\nu 1$, $\nu 2$, and $\nu 5$ exhibit similarities to those in silica particles, implying consistent structural behaviors across different materials, despite compositional differences. Raman depth profiling provided insights into Si–F chemical bonding within SHFS microrods, with bands at 415, 480, and 663 cm^{-1}. This analysis revealed a decrease in the intensity of Si–F stretching vibrational modes toward the microrod's center compared to its surface (Figure 11a). Raman mapping of

https://doi.org/10.1021/acsomega.4c02952
ACS Omega 2024, 9, 24060–24070

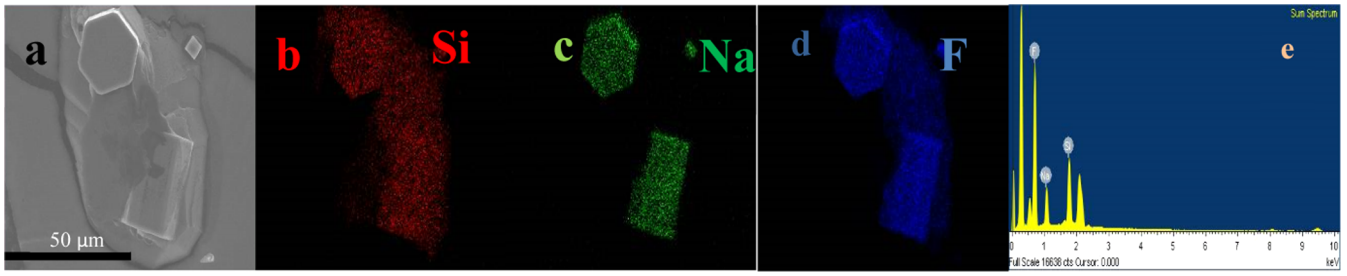

Figure 8. (a–d) FESEM mapping of Na, Si, and F for the SHFS microrod in 0.5 mL of HF. (e) EDX for the SHFS microrod.

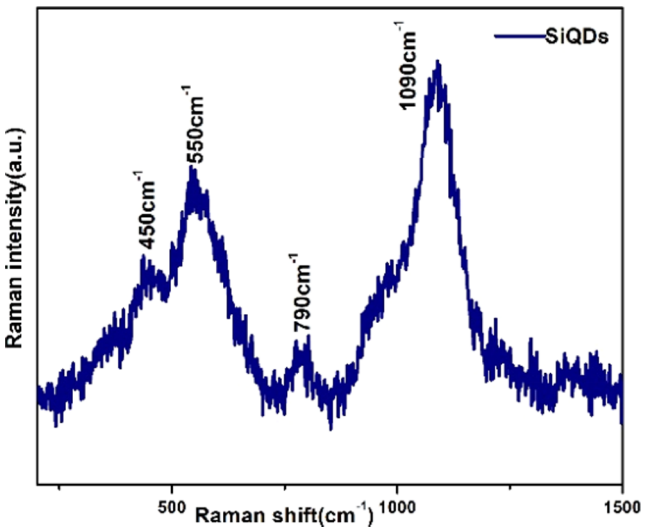

Figure 9. Raman spectrum for film-dried SiQDs.

SHFS microrods illustrated the distribution of Si–F vibrations at 663 cm^{-1}, with a color gradient from deep blue to red indicating the presence and intensity of Si–F vibrations throughout the microrod. Deep blue signifies weaker Si–F vibrations, while red indicates a higher intensity of Si–F vibrations (Figure 11b).[29,37−39]

The absorption and photoluminescence emission spectra of silicon quantum dots (SiQDs) and SHFS microrods dispersed in water are depicted in Figure 12a,b, respectively. The absorption spectrum features a pronounced peak at 332 nm, which is attributed to the SiQDs formation.[23,−43] The shoulder observed at 332 nm is attributed to the Γ–Γ direct bandgap transition. As detailed in Section 2 and illustrated in Figure 12a, the concentration of absorbed hydrofluoric acid (HF) was varied from 0.1 to 1.5 mL. Notably, the distinct excitonic peak at 332 nm diminishes with an increase in HF concentration to 1.5 mL, indicating the instability of SiQDs under strong acidic conditions. This instability leads to the aggregation of quantum dots (QDs). Additionally, a significant transition observed at 265 nm (L-L direct bandgap transition), coupled with a redshift of 20 nm in the 332 nm absorption peak, suggests aggregation of SiQDs and the influence of SHFS presence.[44]

The photoluminescence (PL) emission spectra of silicon quantum dots (SiQDs) were analyzed under an excitation

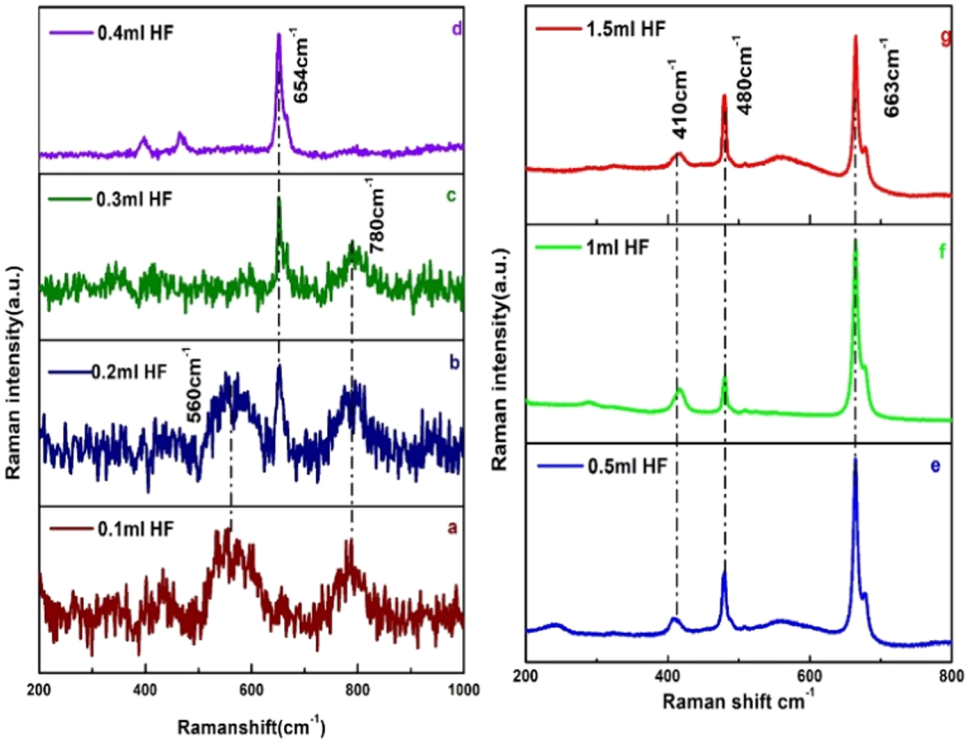

Figure 10. (a–g) Confocal Raman spectra for the formation of the SHFS microrod.

https://doi.org/10.1021/acsomega.4c02952
ACS Omega 2024, 9, 24060−24070

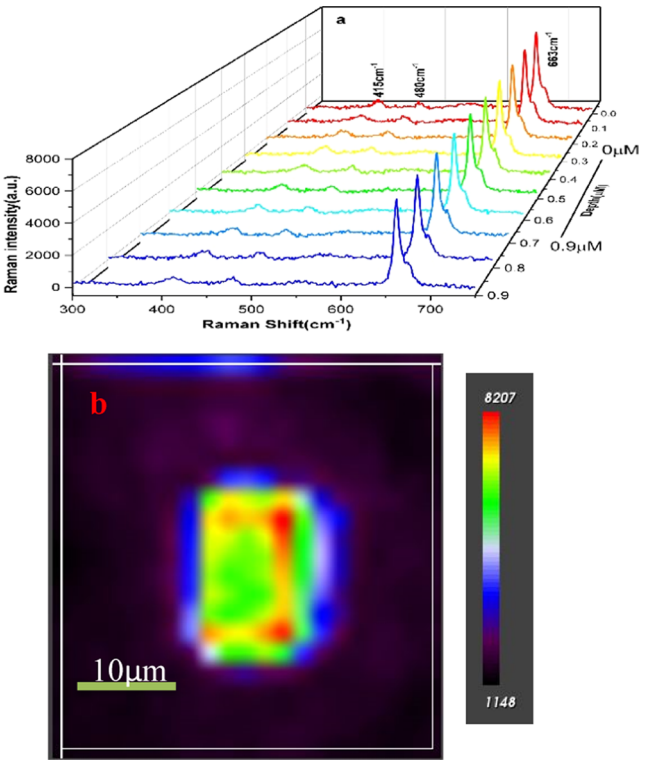

Figure 11. (a) The thickness dependence Raman in-depth profile of SHFS microrod in 0.5 mL of HF. (b) The Si−F vibration mapping of SHFS microrod.

wavelength of 365 nm, revealing a notable peak at 446 nm with a full width at half-maximum (FWHM) of 82 nm, as shown in Figure 12b.[23,45−47] Interestingly, SiQDs initially displayed an excitation-independent spectrum (Figure S9a), and the initial formation of SHFS microrods emission spectra also showed an excitation-independent spectra (Figure S9b−c). However, upon incrementally increasing the concentration of hydrofluoric acid (HF) in the SiQDs solution, a transition to an excitation-dependent spectrum was observed, accompanied by a diminished emission intensity (Figures S9d−f and S10a,b). This shift suggests potential morphological alterations within the SiQDs sample. High-resolution transmission electron microscopy (HR-TEM) analysis revealed the formation of cluster-like structures and the presence of SHFS microrods, indicating an intriguing mechanism of nanoparticle-mediated crystal growth. During the HF concentration process, these quantum dots tend to aggregate and fuse along nonclassical crystallographic directions, facilitating a network of crystal development.

In the context of SiQDs, the surface is functionalized with amine groups and the solution pH is maintained at 10. The introduction of varying concentrations of HF into the SiQDs solution results in a significant pH reduction (ranging from 6 to 1), which enhances the acidic environment. This condition prompts neighboring particles to converge, driven by interparticle forces such as van der Waals or electrostatic forces, leading to loosely structured formations with indistinct boundaries.[48] As SiQDs self-assemble into tiny SHFS particles, aggregation occurs, resulting in the formation of sodium hexafluorosilicate. This aggregation facilitates a pathway for photoexcited electron−hole pairs to relax, effectively quenching the PL spectra through a phenomenon known as charge delocalization.[49,50]

Support for the delocalization effect was provided by lifetime measurements of the SiQDs and SHFS microrods samples. The photoluminescence (PL) decay profiles, obtained by exciting at 365 nm, for SiQDs and SHFS microrods were observed at an emission wavelength of 440 nm, as shown in Figure 13. These PL decay traces were accurately fit with biexponential and triexponential models.

$$I(t) = a_1 e_1^{-t/T} + a_2 e_2^{-t/T},\ I(t) = a_1 e_1^{-t/T} + a_2 e_2^{-t/T} + a_3 e_3^{-t/T}$$

The average lifetime can be calculated using

$$\tau = \left(\frac{A_1 {\tau_1}^2 + A_2 {\tau_2}^2}{A_1 \tau_1 + A_2 \tau_2} \right)$$

and

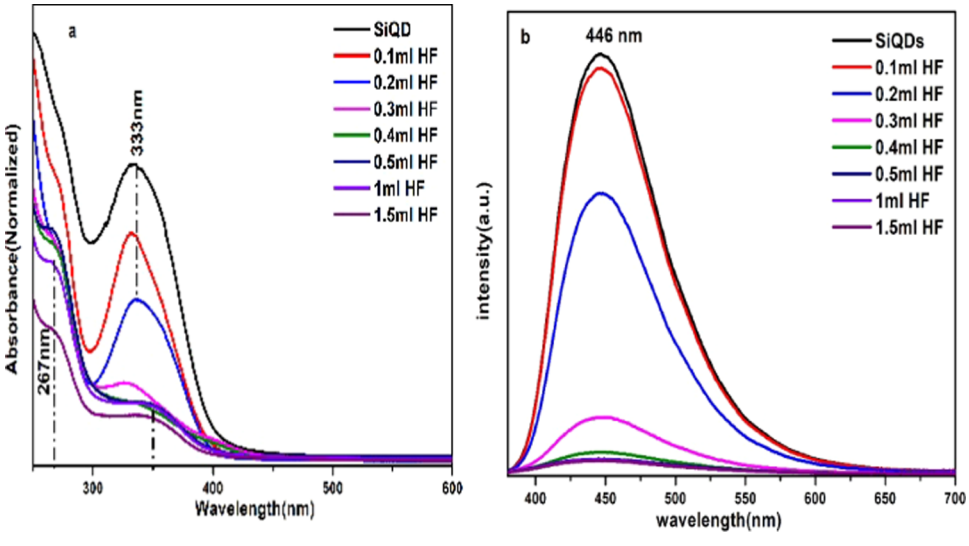

Figure 12. (a) Absorption and (b) emission spectra for the SiQDs and SHFS microrods.

https://doi.org/10.1021/acsomega.4c02952
ACS Omega 2024, 9, 24060−24070

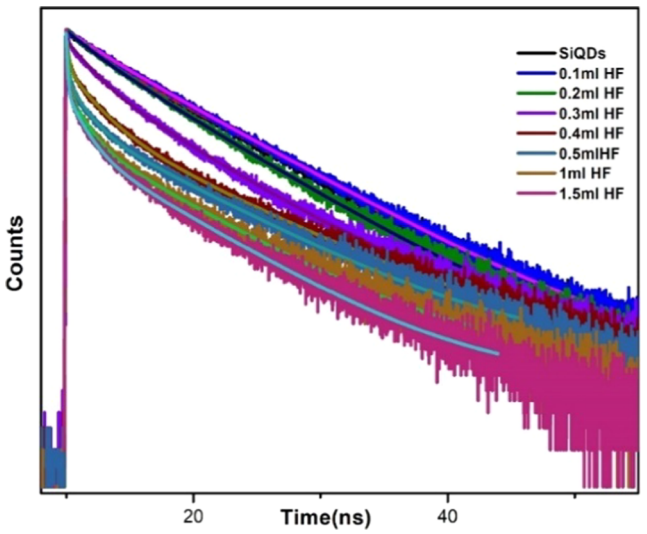

Figure 13. PL lifetime decay for the SiQDs and different HF concentrations (0.1−0.5, 1, and 1.5 mL) for the formation of SHFS microrod.

$$\tau = \left(\frac{A_1\tau_1^{\,2} + A_2\tau_2^{\,2} + A_3\tau_3^{\,2}}{A_1\tau_1 + A_2\tau_2 + A_3\tau_3} \right)$$

t_1, t_2, t_3 is the lifetime, a_1, a_2, a_3 is the amplitude.

The PL decay profiles of SiQDs were subjected to biexponential fitting at low concentrations of hydrofluoric acid (HF) (0.1−0.3 mL). This analysis revealed distinct morphological evolutions: particle nucleation at 0.1 mL HF, self-assembly into flower-like clusters at 0.2 mL HF, and the emergence of hexagonal shapes at 0.3 mL HF. For higher HF concentrations (0.4−1.5 mL), a triexponential function was employed to fit the emission decay curves, reflecting the complex dynamics at play. Notably, at these concentrations, nanoparticle aggregation led to the formation of SHFS microrods, with microrod nucleation initiating at 0.4 mL of HF. A transition in morphology from SiQDs to SHFS microrods was accompanied by a decrease in the average PL lifetime from 7 to 6 ns. The contributions of different lifetime components for both SiQDs and SHFS structure are systematically cataloged in Table S1.

The radiative recombination process, typically characterized by longer fluorescence lifetimes, was found to be enhanced by electron-rich ligands in SiQDs, as corroborated by prior studies.[51,52] The incorporation of HF, however, resulted in a reduction of this lifetime, implicating the role of HF in promoting QD aggregation and fusion, which, in turn, affects the PL properties.

Detailed analysis of the lifetime components and their respective contributions elucidates that varying HF concentrations are instrumental in the formation of SHFS microrods. These structures presumably expedite the localization of excited charge carriers in the proximity of the QDs, consequently reducing the fluorescence lifetime.

4. CONCLUSIONS

We have elucidated the intricate formation mechanism of sodium hexafluorosilicate (SHFS) microrods, unveiling a nonclassical crystal growth process mediated by silicon quantum dots (SiQDs). Our comprehensive study offers compelling evidence supporting the transformation of SiQDs into SHFS flower-like aggregates, the subsequent involvement of primary silica particles in intermediary stages, and ultimately their fusion to yield the final microrod morphology. This work highlights the crucial role of hydrofluoric (HF) acid in driving microrod formation, as corroborated by PXRD and single-crystal X-ray diffraction analyses confirming the presence of SHFS. Notably, the strong fluorescence exhibited by SiQDs is effectively quenched upon SHFS formation. This phenomenon, along with the observed reduction in the photoluminescence (PL) lifetime of the SHFS rod, can be attributed to electron delocalization.

ASSOCIATED CONTENT

Supporting Information

The Supporting Information is available free of charge at https://pubs.acs.org/doi/10.1021/acsomega.4c02952.

The characterization data of the SAED pattern of the SiQDs; histogram of the particle size distribution for SiQDs; FESEM images and mapping of SHFS rods; Raman microscopy images of SHFS microrods; fluorescence microscopy images for all HF concentrations; photoluminescence emission spectra of SiQDs; and all HF concentrations of SiQDs; the lifetime values cataloged for SiQDS and SHFS (PDF)

AUTHOR INFORMATION

Corresponding Author

Devaraj Nataraj − *Quantum Materials & Devices Laboratory, Department of Physics and UGC−CPEPA Centre for Advanced Studies in Physics for the Development of Solar Energy Materials and Devices, Department of Physics, Bharathiar University, Coimbatore, Tamil Nadu 641046, India;* orcid.org/0000-0002-4711-8263; Email: de.nataraj@buc.edu.in

Authors

Maheswari Palanivel − *Quantum Materials & Devices Laboratory, Department of Physics, Bharathiar University, Coimbatore, Tamil Nadu 641046, India;* orcid.org/0009-0004-6739-1269

Thankappan Thrupthika − *Quantum Materials & Devices Laboratory, Department of Physics, Bharathiar University, Coimbatore, Tamil Nadu 641046, India*

Subramaniam Ramya − *Quantum Materials & Devices Laboratory, Department of Physics, Bharathiar University, Coimbatore, Tamil Nadu 641046, India*

Sellan Premkumar − *Joint International Research Laboratory of Information Display and Visualization, School of Electronics Science and Technology, Southeast University, Nanjing 210009, China;* orcid.org/0000-0001-9065-2130

T. Daniel Thangadurai − *KPR Institute of Engineering and Technology, Coimbatore, Tamil Nadu 641407, India*

Complete contact information is available at: https://pubs.acs.org/10.1021/acsomega.4c02952

Author Contributions

Authors M.P. and D.N. conceptualized the idea. M.P. standardized all protocols, prepared SiQDs and SHFS samples performed optical, morphological, and structural characterization, and collected and analyzed the data. T.T., S.P., and S.R. supported the optical analysis. T.D.T. contributed to the

https://doi.org/10.1021/acsomega.4c02952
ACS Omega 2024, 9, 24060−24070

PXRD characterization support. M.P. and D.N. wrote the entire manuscript, and all of the coauthors reviewed and provided critical comments.

Notes

The authors declare no competing financial interest.

■ ACKNOWLEDGMENTS

Author D.N. acknowledges the RUSA 2.0-BCTRC, for providing research funding under RUSA scheme. We are grateful to Prof. Anindya Datta, Department of Chemistry at IIT Bombay for providing scientific and technical support.

■ REFERENCES

(1) Feng, X.; Gao, R.; Wang, R.; Zhang, G. Non-classical Crystal Growth on a Hydrophobic Substrate: Learning from Bivalve Nacre. *CrystEngComm* **2020**, *22*, 3100−3105.

(2) De Yoreo, J. J.; Gilbert, P. U. P. A.; Sommerdijk, N. A. J. M.; Penn, R. L.; Whitelam, S.; Joester, D.; Zhang, H.; Rimer, J. D.; Navrotsky, A.; Banfield, J. F.; et al. Crystallization by Particle Attachment in Synthetic, Biogenic, and Geologic Environments. *Science* **2015**, *349* (6247), No. aaa6760.

(3) Gilbert, P. U. P. A.; Porter, S. M.; Sun, C. Y.; Xiao, S.; Gibson, B. M.; Shenkar, N.; Knoll, A. H. Biomineralization by Particle Attachment in Early Animals. *Proc. Natl. Acad. Sci. U.S.A.* **2019**, *116* (36), 17659−17665.

(4) Fu, H.; Gao, X.; Zhang, X.; Ling, L. Recent Advances in Nonclassical Crystallization: Fundamentals, Applications, and Challenges. *Cryst. Growth Des.* **2022**, *22* (2), 1476−1499.

(5) Miyamoto, H.; Miyashita, T.; Okushima, M.; Nakano, S.; Morita, T.; Matsushiro, A. A Carbonic Anhydrase from the Nacreous Layer in Oyster Pearls. *Proc. Natl. Acad. Sci. U.S.A.* **1996**, *93* (18), 9657−9660.

(6) Falini, G.; Albeck, S.; Weiner, S.; Addadi, L. Control of Aragonite or Calcite Polymorphism by Mollusk Shell Macromolecules. *Science* **1996**, *271*, 67−69.

(7) Feng, X.; Zhang, G. New Insights into the Spatial Confinement Mechanism of Nucleation of Biogenic Aragonite Crystals from Bivalve Nacre. *CrystEngComm* **2020**, *22* (40), 6596−6602.

(8) Mcginty, J.; Yazdanpanah, N.; Price, C.; Horst, J.; Sefcik, J. Nucleation and Crystal Growth in Continuous Crystallization. In *The Handbook of Continuous Crystallization*, 1st ed.; Royal Society of Chemistry, 2020; Chapter 1.

(9) Takasaki, M.; Kimura, Y.; Yamazaki, T.; Oakia, Y.; Imai, H. 1D oriented attachment of calcite nanocrystals: formation of single-crystalline rods through collision. *RSC Adv.* **2016**, *6*, 61346−61350.

(10) Cölfen, H.; Mann, S. Higher-Order Organization by Mesoscale Self-Assembly and Transformation of Hybrid Nanostructures. *Angew. Chem., Int. Ed.* **2003**, *42* (21), 2350−2365.

(11) De Yoreo, J. J.; Vekilov, P. G. Principles of Crystal Nucleation and Growth. *Rev. Mineral. Geochem.* **2003**, *54* (1), 57−93.

(12) Penn, R. L.; Banfield, J. F. Morphology development and crystal growth in nanocrystalline aggregates under hydrothermal conditions: Insights from titania. *Geochim. Cosmochim. Acta* **1999**, *63*, 1549−1557.

(13) Wang, H.; Liu, Y.; Liu, Z.; Xu, H. M.; Deng, Y. J.; Shen, H. Hierarchical rutile TiO_2 mesocrystals assembled by nanocrystals-oriented attachment mechanism. *CrystEngComm* **2012**, *14*, 2278−2282.

(14) Zong, Y.; Liu, Y.; Zhao, W.; Zhang, H.; Li, B.; Zhou, X.; Shen, H. Chitosan-Assisted Assembly of Sub-10 Nm Nanocrystals into Mesoporous TiO_2 Fibers with High-Aspect-Ratio for Improved Lithium-Ion Storage. *Electrochim. Acta* **2015**, *180*, 658−665.

(15) Niederberger, M.; Cölfen, H. Oriented Attachment and Mesocrystals: Non-Classical Crystallization Mechanisms Based on Nanoparticle Assembly. *Phys. Chem. Chem. Phys.* **2006**, *8* (28), 3271−3287.

(16) Cölfen, H.; Antonietti, M. Mesocrystals: Inorganic Superstructures Made by Highly Parallel Crystallization and Controlled Alignment. *Angew. Chem., Int. Ed.* **2005**, *44*, 5576−5591.

(17) Schliehe, C.; Juarez, B. H.; Pelletier, M.; Jander, S.; Greshnykh, D.; Nagel, M.; Meyer, A.; Foerster, S.; Kornowski, A.; Klinke, C.; Weller, H. Ultrathin PbS Sheets by Two-Dimensional Oriented Attachment. *Science* **2010**, *329*, 550−553.

(18) Koh, W.-K.; Bartnik, A. C.; Wise, F. W.; Murray, C. B. Synthesis of Monodisperse PbSe Nanorods: A Case For Oriented Attachment. *J. Am. Chem. Soc.* **2010**, *132*, 3909−3913.

(19) Pacholski, C.; Kornowski, A.; Weller, H. Self-assembly of ZnO: From nanodots, to nanorods. *Angew. Chem., Int. Ed.* **2002**, *41*, 1188−1191.

(20) Zitoun, D.; Pinna, N.; Frolet, N.; Belin, C. Single Crystal Manganese Oxide Multipods by Oriented Attachment. *J. Am. Chem. Soc.* **2005**, *127* (43), 15034−15035.

(21) Pathiraja, G.; Yarbrough, R.; Rathnayake, H. Fabrication of Ultrathin CuO Nanowires Augmenting Oriented Attachment Crystal Growth Directed Self-Assembly of Cu(OH)2 Colloidal Nanocrystals. *Nanoscale Adv.* **2020**, *2*, 2897−2906.

(22) Zhuang, Z.; Huang, F.; Lin, Z.; Zhang, H. Aggregation-induced fast crystal growth of SnO_2 nanocrystals. *J. Am. Chem. Soc.* **2012**, *134* (39), 16228−16234.

(23) Wu, J.; Dai, J.; Shao, Y.; Sun, Y. One-step synthesis of fluorescent silicon quantum dots (Si-QDs) and their application for cell imaging. *RSC Adv.* **2015**, *5*, 83581−83587.

(24) Ji, J.; Wang, G.; You, X.; Xu, X. Functionalized silicon quantum dots by N-vinylcarbazole: synthesis and spectroscopic properties. *Nanoscale Res. Lett.* **2014**, *9*, 384.

(25) Cardinal, T.; Efimov, O. M.; Francois-Saint-Cyr, H. G.; Glebov, L. B.; Glebova, L. N.; Smirnov, V. I. Comparative study of photo-induced variations of X-ray diffraction and refractive index in photo-thermo-refractive glass. *J. Non-Cryst. Solids* **2003**, *325* (1−3), 275−281.

(26) El Agammy, E. F.; Doweidar, H.; El-Egili, K.; Ramadan, R.; Jaremko, M.; Emwas, A. H. Structure of NaF−TeO2 glasses and glass-ceramics. *Ceram. Int.* **2020**, *46* (11), 18551−18561.

(27) Kashiwaya, Y.; Cramb, A. W. Kinetics of formation and dissociation of Na2SiF6. *Metall. Mater. Trans. B* **2002**, *33* (1), 129−136.

(28) Du, N.; Wu, H.; Zhang, H.; Zhai, C.; Wu, P.; Wang, L.; Yang, D. Large-scale synthesis of water-soluble nanowires as versatile templates for nanotubes. *Chem. Commun.* **2011**, *47* (3), 1006−1008.

(29) Zhao, J. Y.; Wang, X. G. Preparation, structure and luminescent performance of Na_2 SiF_6: Re 3+(Re 3+= Eu 3+, Tb 3+, Ce 3+) powders. *Appl. Phys. A* **2019**, *125*, 178 DOI: 10.1007/s00339-019-2468-1.

(30) Zhang, W.; Jing, Q.; Fang, Y.; Chen, Z. Z. Z. Synthesis, structure, and properties of nonlinear optical crystal Na2SiF6. *Z. Anorg. Allg. Chem.* **2017**, *643*, 1739−1743, DOI: 10.1002/zaac.201700322.

(31) Abdelhameed, M.; Martir, D. R.; Chen, S.; Xu, W. Z.; Oyeneye, O. O.; Chakrabarti, S.; Zysman-Colman, E.; Charpentier, P. A. Tuning the optical properties of silicon quantum dots via surface functionalization with conjugated aromatic fluorophores. *Sci. Rep.* **2018**, *8*, No. 3050.

(32) Dasog, M.; Yang, Z. Y.; Regli, S.; Atkins, T. M.; Faramus, A.; Singh, M. P.; Muthuswamy, E.; Kauzlarich, S. M.; Tilley, R. D.; Veinot, J. G. C. Chemical Insight into the Origin of Red and Blue Photoluminescence Arising from Freestanding Silicon Nanocrystals. *ACS Nano* **2013**, *7*, 2676−2685.

(33) Huisken, F.; Hofmeister, H.; Kohn, B.; Laguna, M.; Paillard, V. Laser Production and Deposition of Light-Emitting Silicon Nanoparticles. *Appl. Surf. Sci.* **2000**, *154−155*, 305−313.

(34) Alessi, A.; Agnello, S.; Buscarino, G.; Gelardi, F. M. Structural Properties of Core and Surface of Silica Nanoparticles Investigated by Raman Spectroscopy. *J. Raman Spectrosc.* **2013**, *44*, 810−816.

(35) Rawat, R.; Tiwari, A.; Vendamani, V. S.; Pathak, A. P.; Rao, S. V.; Tripathi, A. Synthesis of Si/SiO_2 nanoparticles using nanosecond

https://doi.org/10.1021/acsomega.4c02952
ACS Omega 2024, 9, 24060−24070

laser ablation of silicate-rich garnet in water. *Opt. Mater.* **2018**, *75*, 350−356.
(36) Guo, C.; Jordan, J. S.; Yarger, J. L.; Holland, G. P. Highly Efficient Fumed Silica Nanoparticles for Peptide Bond Formation: Converting Alanine to Alanine Anhydride. *ACS Appl. Mater. Interfaces* **2017**, *9*, 17653−17661.
(37) Arianpour, F.; Arianpour, A. Ç.; Aali, B. Characterization and Properties of Sodium Hexa-Fluorosilicate and its Potential Application in the Production of Sodium Fluoride. *Silicon* **2021**, *13*, 4381−4389.
(38) Tang, F.; Su, Z.; Ye, H.; Wang, M.; Lan, X.; Phillips, D. L.; Cao, Y.; Xu, S. A Set of Manganese Ion Activated Fluoride Phosphors (A_2BF_6:Mn^{4+}, A = K, Na, B = Si, Ge, Ti): Synthesis below 0 Degrees °C and Efficient Room-Temperature Photoluminescence. *J. Mater. Chem. C* **2016**, *4*, 9561−9568.
(39) Parker, S. F.; Williams, K. P.; Smith, T.; Ramirez-Cuesta, A. J.; Daemen, L. L. Vibrational Spectroscopy of Hexahalo Complexes. *Inorg. Chem.* **2022**, *61* (15), 5844−5854.
(40) Holmes, J. D.; Ziegler, K. J.; Doty, R. C.; Pell, L. E.; Johnston, K. P.; Korgel, B. A. Highly Luminescent Silicon Nanocrystals with Discrete Optical Transitions. *J. Am. Chem. Soc.* **2001**, *123*, 3743−3748.
(41) Dohnalová, K.; Poddubny, A. N.; Prokofiev, A. A.; de Boer, W. D. A. M.; Umesh, C. P.; Paulusse, J. M. J.; Zuilhof, H.; Gregorkiewicz, T. Surface Brightens Up Si Quantum Dots: Direct Bandgap-Like Size-Tunable Emission. *Light: Sci. Appl.* **2013**, *2*, No. e47.
(42) Hu, G.; Sun, Y.; Xie, Y.; Wu, S.; Zhang, X.; Zhuang, J.; Hu, C.; Lei, B.; Liu, Y. Synthesis of Silicon Quantum Dots with Highly Efficient Full-Band UV Absorption and Their Applications in Antiyellowing and Resistance of Photodegradation. *ACS Appl. Mater. Interfaces* **2019**, *11*, 6634−6643.
(43) Wang, L.; Li, Q.; Wang, H.-Y.; Huang, J.-C.; Zhang, R.; Chen, Q.-D.; Xu, H.-L.; Han, W.; Shao, Z.-Z.; Sun, H.-B. Ultrafast Optical Spectroscopy of Surface-Modified Silicon Quantum Dots: Unraveling the Underlying Mechanism of the Ultrabright and Color-Tunable Photoluminescence. *Light: Sci. Appl.* **2015**, *4*, e245−e253.
(44) Yuan, S.; Heng, X.; Zhang, Q.; Hu, J. pH-induced aggregation growth of large Au nanoparticles from zwitterionic ligand-modified small Au nanoparticles. *Colloids Surf., A* **2016**, *506*, 6−12.
(45) Warner, J. H.; Rubinsztein-Dunlop, H.; Tilley, R. D. Surface Morphology Dependent Photoluminescence from Colloidal Silicon Nanocrystals. *J. Phys. Chem. B* **2005**, *109*, 19064−19067.
(46) Roy, D.; Majhi, K.; Mondal, M. K.; Saha, S. K.; Sinha, S.; Chowdhury, P. Silicon quantum dot-based fluorescent probe: synthesis characterization and recognition of thiocyanate in human blood. *ACS Omega* **2018**, *3* (7), 7613−7620.
(47) Cheng, X.; Lowe, S. B.; Reece, P. J.; Gooding, J. J. Colloidal Silicon Quantum Dots: From Preparation to the Modification of Self-Assembled Monolayers (Sams) for Bio-Applications. *Chem. Soc. Rev.* **2014**, *43*, 2680−2700.
(48) Li, H.; Fan, J.; Cui, W. Nanoparticle-mediated nonclassical crystal growth of sodium fluorosilicate nanowires and nanoplates. *AIP Adv.* **2011**, *1* (4), No. 042165.
(49) Premkumar, S.; Nataraj, D.; Bharathi, G.; Khyzhun, O. Y.; Thangadurai, T. D. Interfacial Chemistry-Modified QD-Coupled CdTe Solid Nanowire and Its Hybrid with Graphene Quantum Dots for Enhanced Photocurrent Properties. *ChemistrySelect* **2017**, *2*, 10771−10781.
(50) Ramya, S.; Nataraj, D.; Krishnan, S.; Premkumar, S.; Thrupthika, T.; Sangeetha, A.; Senthilkumar, K.; Thangadurai, T. D. Aggregation Induced Emission Behavior in Oleylamine Acetone System and Its Application to Get Improved Photocurrent from In_2S_3 Quantum Dots. *Sci. Rep.* **2020**, *10*, No. 19712.
(51) Chatterjee, S.; Mukherjee, T. K. Thermal Luminescence Quenching of Amine-Functionalized Silicon Quantum Dots: a pH and Wavelength-Dependent Study. *Phys. Chem. Chem. Phys.* **2015**, *17* (37), 24078−24085.
(52) De los Reyes, G. B.; Dasog, M.; Na, M.; Titova, L. V.; Veinot, J. G.; Hegmann, F. A. Charge transfer state emission dynamics in blue-emitting functionalized silicon nanocrystals. *Phys. Chem. Chem. Phys.* **2015**, *17* (44), 30125−30133.

https://doi.org/10.1021/acsomega.4c02952
ACS Omega 2024, 9, 24060−24070